Supplementary Information to

Calmodulin as a Direct Detector of Ca^{2+} Signals

by Guido C. Faas, Sridhar Raghavachari, John E. Lisman, and Istvan Mody

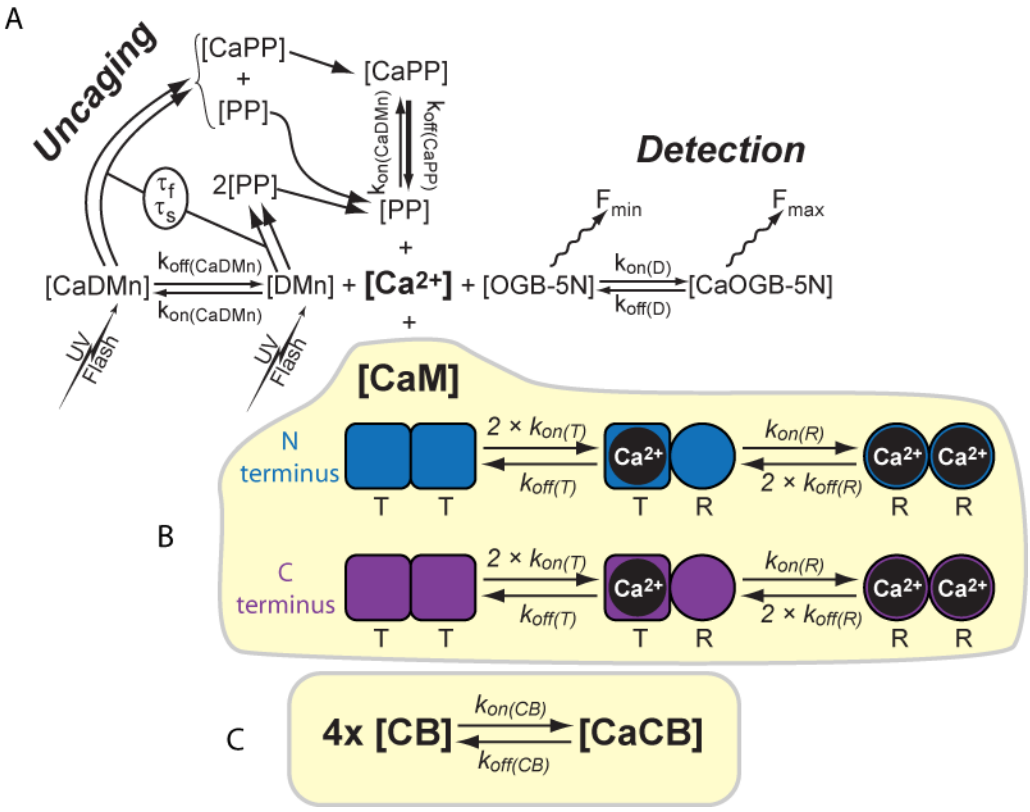

Supplementary Figure 1. Schematics of the simulated reactions. A) To determine the kinetics of the binding of Ca^{2+} to CaM we used a mathematical model that simulated all processes occurring in the reaction chamber. The properties of DMn, its photoproducts (PP) and OGB-5N were determined in independent experiments. The properties of CaM and CB were determined by fitting the uncaging data with the mathematical model. B) CaM contains two high affinity Ca^{2+}-binding sites on its C terminus and two lower affinity sites on its N terminus. The steady-state affinity for Ca^{2+} of these sites has been measured in several ways. These (and other) measurements indicate that each pair has positive cooperativity. We incorporated cooperativity in the model by including an allosteric effect, as shown. In our model, the cooperativity is based on the ability of the binding sites to occur in two states, one with a low affinity for Ca^{2+} (T) and one with a high affinity (R). A binding site is in the T state, when the other binding site in the cooperative pair has no Ca^{2+} bound. A binding site is in the R state, when the other site has Ca^{2+} bound. In this model, the transitions from T to R and vice versa are considered to occur instantaneously. This type of model has been used successfully to simulate kinetics of cooperative binding sites in calretinin[35] and gives an intuitive insight into the kinetics of cooperative binding. **C)** For CB there are no indications that there are cooperative interactions between its four binding sites. Therefore, CB was modeled as having four independent binding sites. A model with all four sites being identical resulted in acceptable fits.

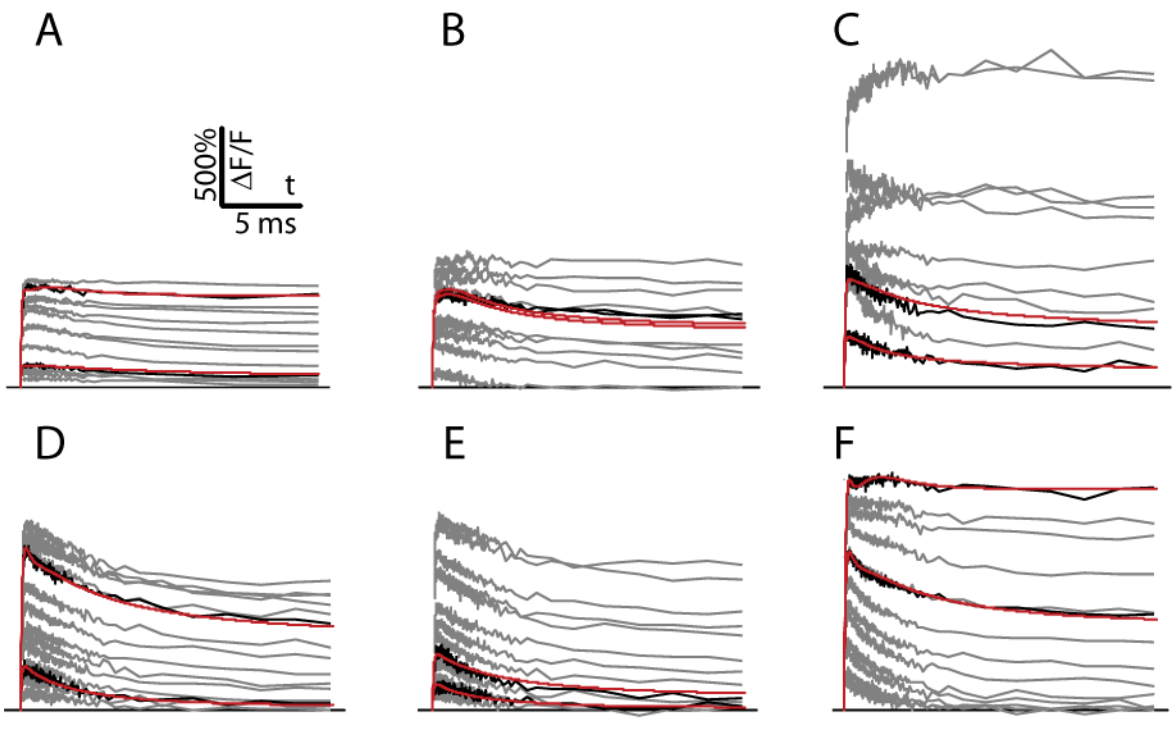

Start conditions

Set	[DMn]	[OGB-5N]	$[Ca^{2+}]_{free}$	[CaM]
A	5.56 mM	50 μM	1.88 μM	123 μM
B	3.64 mM	100 μM	1.10 μM	143 μM
C	3.64 mM	100 μM	730 nM	72 μM
D	3.64 mM	50 μM	255 nM	187 μM
E	3.64 mM	50 μM	410 nM	140 μM
F	3.64 mM	50 μM	399 nM	94 μM
G	3.64 mM	50 μM	394 nM	47 μM

Supplementary Figure 2. Examples of fitted data sets. All individual Ca^{2+} transients for the experiments with CaM were grouped according to the experimental conditions indicated in the Table (inset). The black traces are examples of one of the randomly picked datasets that were fitted simultaneously. The red lines are the actual fits for that set. Scale bars in A apply to all datasets.

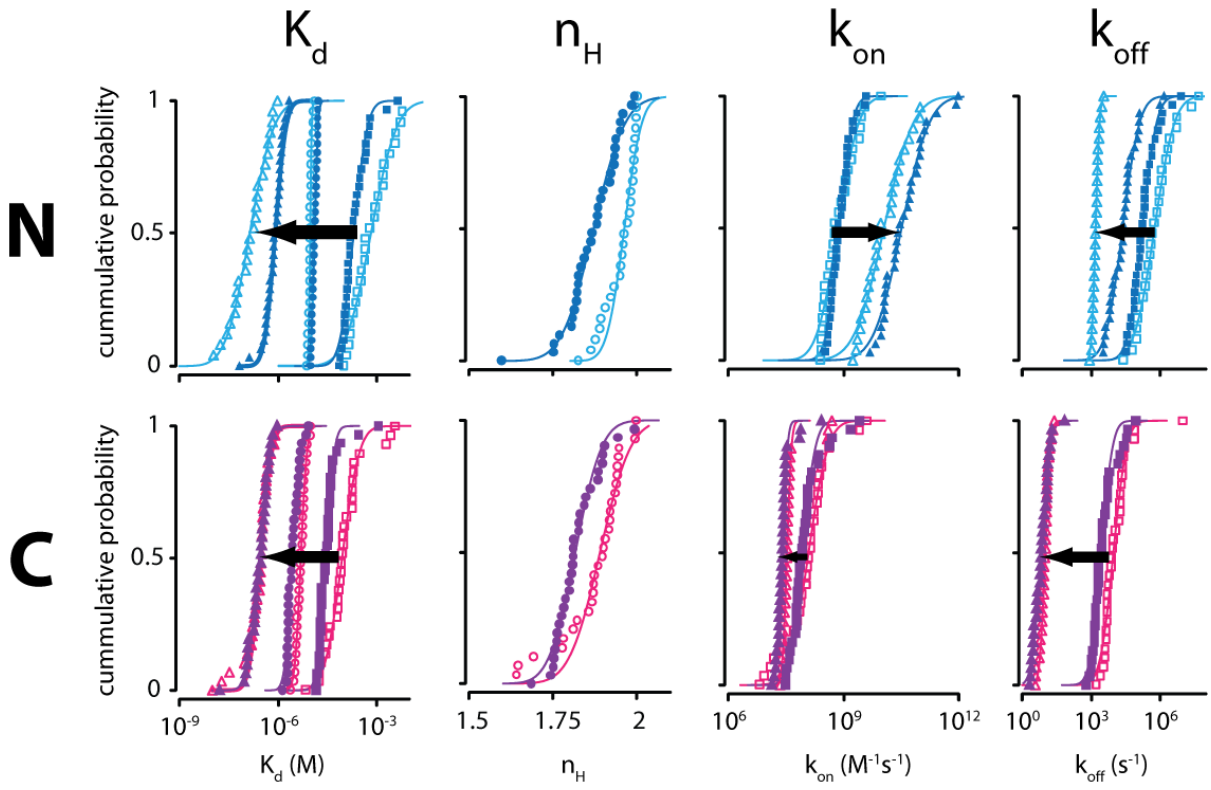

Supplementary Figure 3. Ca^{2+} binding properties of CaM accumulated from each fitted set. Cumulative probability plots of the fitted results (fitted parameters) for wild type CaM (filled symbols) and mutants (open symbols). The fast and low affinity cooperative pair measured in the wildtype CaM data (dark blue filled symbols) is grouped with the CaM_{EF34} data (light blue open symbols) based on comparable values indicating that the fast, low affinity pair represents the N-lobe (**N**). Similarly, the slower, high affinity cooperative pair measured in wildtype CaM (purple filled symbols) is grouped with the CaM_{EF12} data (pink open symbols) based on comparable values indicating that the slower, high affinity pair represents the C-lobe (**C**). Arrows indicate the transition from T-state (square symbols) to R state (triangular symbols) as Ca^{2+} binds. The circular symbols in the K_d graphs indicate the apparent K_d (equivalent to a steady state binding curve). The solid lines are fits with a log-normal distribution function for which the results can be found in Table 1 of the main text.

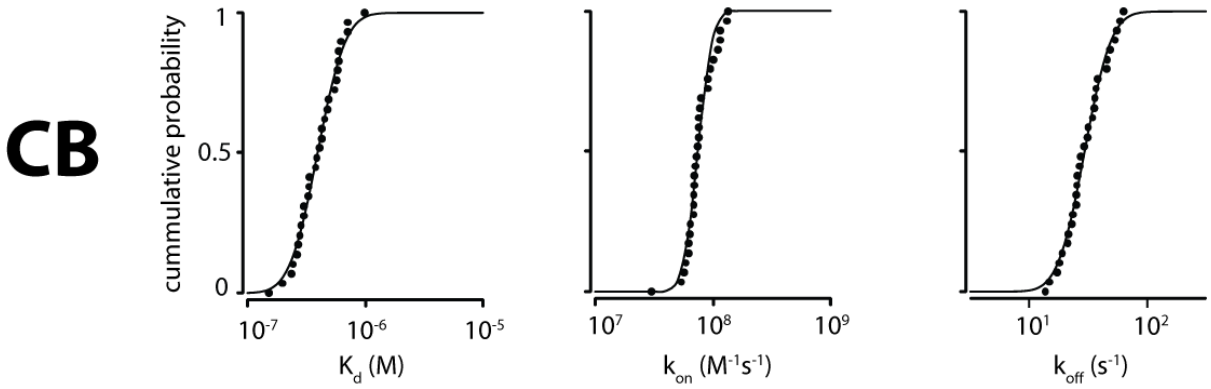

Supplementary Figure 4. Ca^{2+} binding properties of CB. Shown are the fitted results (fitted parameters) of all the randomly chosen sets of CB traces as cumulative probability plots. The solid lines are fits with a log-normal distribution function for which the results can be found in the main text.

Fit round 1

$$\left\{\begin{matrix} Set_1 \\ \vdots \\ Set_n \end{matrix}\right\} loose\ \ fit \overset{\text{Start values}}{\left\{\begin{matrix} {}^1Group_1 \\ \vdots \\ {}^1Group_m \end{matrix}\right\}} \Rightarrow \overset{\text{Fitted values}}{\left\{\begin{matrix} {}^2Group_1 \\ \vdots \\ {}^2Group_p \end{matrix}\right\}}$$

Fit round 2

$$\left\{\begin{matrix} Set_1 \\ \vdots \\ Set_n \end{matrix}\right\} stiff\ \ fit \overset{\text{Start values}}{\left\{\begin{matrix} {}^2Group_1 \\ \vdots \\ {}^2Group_p \end{matrix}\right\}} \Rightarrow \overset{\text{Fitted values}}{\left\{\begin{matrix} {}^3Group_1 \\ \vdots \\ {}^3Group_{n\times p} \end{matrix}\right\}} \rightarrow \overset{\text{Fitted values}}{\left\{\begin{matrix} Collection_1 \\ \vdots \\ Collection_p \end{matrix}\right\}}$$

where $Collection_x \in \bigcup_{i=1}^{n} {}^3Group_{x,\text{Set}\,i}$

Supplementary Figure 5. Fitting procedure to explore the entire parameter space. In fitting round #1) all sets are fitted with a variety of starting values for the parameters (^{1}Groups, ~20 groups). The fit procedure is set such that the parameters can make large swings during the fitting (loose fit). These first fits give groups of parameters (^{2}Groups) that each can describe one or more sets. Groups with very similar values for every parameter are made into a single group by averaging the individual parameters. In fitting round #2) every set is fitted with the ^{2}Groups as starting values. The fit procedure is set such that the parameters can make only small deviations during the fitting, forcing the model to find a solution with most (if not all) of the parameters close to their initial values (stiff fit). This results in a collection of groups for each set of fits in which the parameters can be determined with a certain distribution. If a collection had one or more parameters with a wide distribution (multiple orders of magnitude), the results were assumed to stem from a local minimum in error space with invalid parameter values.

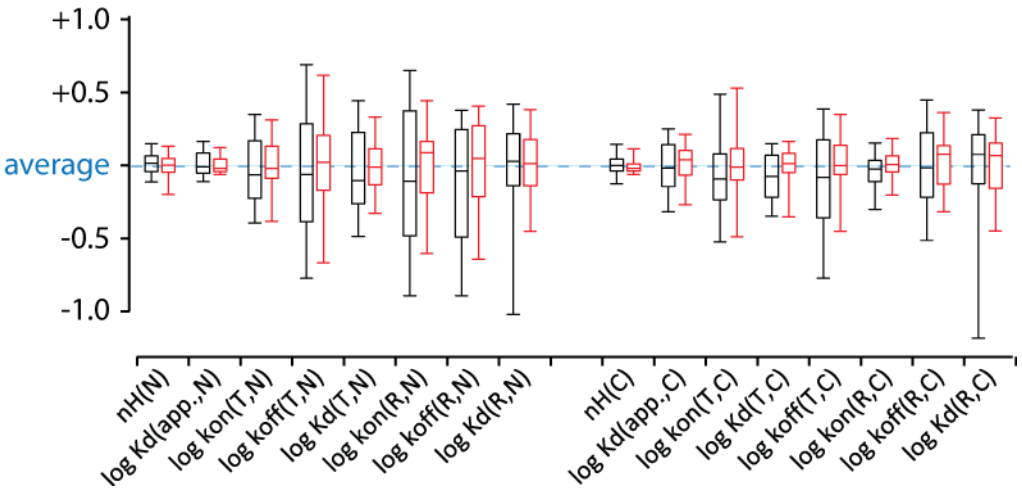

Supplementary Figure 6. Box and whiskers plots of the fitted parameters lined up at their averages. The spread of all the fits (black) (*i.e.*, the data from Supplementary Fig. 3) can be compared to the spread caused by random deviation of ±5% in the constant parameters (see text for details) of fits to 2 sets of curves from the same dataset (red). The variations caused by deviations of parameters assumed to be constant are comparable or smaller than those caused by other factors inherent to the whole experiment (red boxes are smaller than the black ones).

Supplementary data 1. Diffusion limit

The rate constant we found for the association rate of the N-lobe binding sites in the R-state is extremely fast (3.2×10^{10} $M^{-1}s^{-1}$). To ascertain whether this was theoretically possible, we calculated the diffusion limited reaction speed for CaM and Ca^{2+} based on the rate of intermolecular collisions. Using the Smoluchowski theory and the Einstein–Smoluchowski relation[26,27]:

$$k_{diffusion} = 4\pi\left(r_A + r_B\right)\left(D_A + D_B\right)N_A \times 10^3 \quad M^{-1}s^{-1}$$

$$D = \frac{k_B T}{6\pi\eta r} \quad m^2 s^{-1}$$

$R_{Ca(^{2+})}$ = 1.14 Å

r_{CaM} = 25 Å

N_A = 6.022×10^{23} mol^{-1}

k_B = 1.3807×10^{-23} JK^{-1}

T = 308 K

$\eta_{water,308K}$ = 7.25×10^{-4} Pa s

We find a rate limit of 5.6×10^{10} $M^{-1}s^{-1}$ for our conditions (35°C in aqueous solution), indicating that our determined rate of 3.2×10^{10} $M^{-1}s^{-1}$ is theoretically possible.

Supplementary data 2. Fit results of CB compared to earlier experiments

Berggard et al.[1] reported some cooperativity in the binding of Ca^{2+} to CB while we found that the simplest model without any cooperativity fit the data quite well. However, the cooperativity found by Berggard et al. [1] is actually quite small. We calculated from their described Adair binding curves an n_H of 1.2–1.3. We incorporated this small cooperativity but found that the fit results were indistinguishable from using no cooperativity. This makes it impossible to confirm or reject the existence of such small cooperativity with our system. We chose to use the model without cooperativity as it is the least complex (least number of parameters to be fitted), making the fit results more reliable (less degrees of freedom). Furthermore, the cooperativity described by Berggard et al.[1] could be different from ours because of the difference of temperature ath which the experiments were performed (theirs was conducted at 20–25°C, ours at 35°C).

In other earlier measurements[2] we found similar kinetics and steady state binding affinity for CB as reported here, but we also found that CB has at least one different binding site with different kinetics. Besides the difference in temperature at which these experiments were preformed (20°C), it is also likely that an improvement of the fitting model underlies this difference. In our earlier measurements on CB, we did not consider the detailed kinetic uncaging properties of DMn[3] and assumed that DMn uncaged with a single time constant.

Supplementary data 3. Quantification of Ca^{2+} buffering capacity (κ)

The buffering capacity κ is defined as[22] the increase in the Ca^{2+} that is bound to buffers in a system relative to the amount of Ca^{2+} that will stay unbound upon a change in total Ca^{2+} of that system:

$$\kappa = \frac{d[CaB]}{d[Ca^{2+}]} \qquad \text{(eq. S7)}$$

Strictly this means that κ should quantify the full Ca^{2+}-buffering capacity of a system, irrespective of the buffering speed. However, in practice it is used to describe only the fast buffering capacity of a system. Generally, κ is determined using the 'added buffer' approach[22,23,24]. With this method one determines the $\Delta[Ca^{2+}]_{total}$ that is undetectable by the used dye due to the fast buffering of the system. It describes how much bigger the portion of ΔCa^{2+} that is rapidly bound by buffers in the system compared to the maximum portion that is detected by the dye. To compare κ's (determined by the added buffer method) between two experiments, one has to use dyes with similar kinetics because κ expresses the buffer capacity that is faster than the indicator. A faster indicator will yield a smaller κ. The decay in $[Ca^{2+}]$ that is detected by the dye after the peak in measured $[Ca^{2+}]$ is generally considered to result from slower mechanisms of $[Ca^{2+}]$ regulation (*e,g,*, extrusion) and is therefore not included in κ (even if it is binding of Ca^{2+} to a buffer).

Supplementary data 4. Neuronal CaM Concentration

Our simulation used a [CaM] of 100 μM. If CaM is reduced in the simulation from 100 μM to 50, 25 or 0 μM the κ of the system with 30 μM CB reduces from 19 to 10, 5 or 1, respectively. If instead CB is taken out of the simulation, the κ of the system with 100 μM CaM reduces to 12. These results indicate that the fast buffering property of the whole system is directly dependent on CaM while the slower CB can only add to κ when a fast component is in place. This indicates that CaM is essential for the fast buffering in this system and not merely the dominant fast buffer because of its high concentration. The measured fast buffer capacity of spines is ~20[4,5] which can be well accounted for by 100 μM CaM. Thus, if 100 μM CaM is an overestimate of the [CaM] in a spine, there must be an additional molecular species contributing to fast buffering. Thus far it has been challenging to directly measure the intracellular CaM concentration. However, many studies have measured the soluble fraction of CaM from brain homogenates relative to the total protein content (supplementary Table 1), which varies based on the specific brain region and species. Based on values from human, rat and bovine for CaM (μg/mg protein) and the total protein content (~10%[6,7,8]), we estimated the range of intracellular [CaM] (CaM (μM), supplementary Table 1) assuming that the soluble fraction should be dissolved in the water content of the brain (~77%). This value could be further refined by the assumption that all soluble CaM came from intracellular content (~80%). This volume corrected [CaM] (vol. corrected CaM (μM), supplementary Table 1) varied between 31 and 337 μM. The large variation is mainly caused by the outliers for the reported CaM content in brain homogenates. We also calculated the [CaM] based on the median reported CaM content per brain region (green numbers, supplementary Table 1) and found the [CaM] varied from ~65 μM for the cerebellum to 152 μM for the caudate nucleus. Therefore, in our simulation of a spine in the hippocampus, a [CaM] of 100 μM might actually be an underestimate, especially when one considers that CaM could be enriched in specific cellular compartments[9,10]. Although these considerations are important in determining the role of CaM as the fast buffer, the absolute [CaM] is not essential to our discussion considering the activation of CaM or its individual lobes in a nano-domain. There we discussed the probability of a single CaM molecule being activated independent of the overall [CaM].

Supplementary Table 1. Calculation of neuronal CaM concentration

	Water (w/w %)	Protein (w/w %)	soluble CaM (µg/mg protein)	soluble CaM[a] (w/w %)	CaM[b] (µM)	extracell. vol.[11] (%)	CaM vol. corrected[c] (µM)
Whole Brain	77–78[6] 77.8[12] 76–78[13]	8[6] 8–13[7] 9–10[8]					
Cerebrum/ Cerebral cortex			15.9[14] 16.9–17.8[15] 14–15[16] 13[17] 14[18] 13.7–13.8[19] 20.9[20]	0.104–0.272	80–214 112[e]	18–20	97–268 141[f]
Cerebellum			11.2[15] 4[16] 9.5[21] 6[18] 7.5–7.7[19] 18.1[20]	0.032–0.235	25–185 52[e]	21–31	31–268 65[f]
Hippocampus			14.3[14] 15.2[15] 12[16]	0.096–0.198	74–156 111[e]	22	94–200 139[f]
Caudate nucl.			15.2[14] 16.2[15]	0.122–0.211	94–166 122[e]	21	119–210 152[f]
Striatum			15[16] 8[17] 26.4[20]	0.064–0.343	49–270 117[e]		61–337[d] 146[f]
Amygdala			13[16]	0.104–0.169	80–133 101[e]		100–166[d] 126[f]

[a]) $\text{soluble CaM (w/w \%)} = \frac{\text{soluble CaM } (\mu\text{g/mg protein})/10}{100} \times \text{Protein (w/w \%)}$ (eq. S4)

[b]) $\text{CaM } (\mu\text{M}) = \frac{\text{soluble CaM } (\mu\text{g/mg protein}) \times 10}{16.7\text{kDa} \times \left(\text{water (w/w \%)}/100\right)}$ (eq. S5)

[c]) $\text{vol. corrected CaM } (\mu\text{M}) = \frac{\text{CaM } (\mu\text{M})}{1 - \left(\text{extracell. vol.(w/w \%)}/100\right)}$ (eq. S6). An overall brain density of 1 g/ml was assumed, based on published volume and weight data[6].

[d]) For these calculations 20% extracellular was used, estimated from the values of the other regions.

[e]) Value calculated using 77% water (w/w %), 10% protein (w/w %) and the median value for CaM (µg/mg protein).

[f]) Values calculated using values from e) and a extracellular volume of 20%.

Supplementary data 5. Simulating 1 yM dye to measure [Ca^{2+}]

In a simulation the [Ca^{2+}] can be directly determined and does not have to be measured as such. However, to make a comparison with what would be measured in real measurements in cells, we calculated the Ca^{2+} signal that would be measured by adding to our simulation 1 yM (10^{-24} M) of OGB-1 (Fig. 2a, K_d=170 nM, k_{on}=10^9 $M^{-1}s^{-1}$), a dye often used for Ca^{2+} measurements in neurons. Such small concentration of OGB-1 is impossible to use in a real experiment. However, in a simulation it will not influence the actual [Ca^{2+}] but can still be used to reflect the limit of [Ca^{2+}] that would be imposed by the kinetic properties of OGB-1 in a real experiment ([Ca^{2+}]$_{OGB-1}$)[5,25]. In our simulation, the [Ca^{2+}]$_{OGB-1}$ has a peak amplitude of 2.5 μM. The limit of [Ca^{2+}] that could be measured with a dye in a real experiment is basically what is determined with the 'added buffer' approach used to determine κ [22,23,24]. By measuring the [Ca^{2+}] under different Ca^{2+} indicator concentrations one interpolates the [Ca^{2+}] that would be measured with no indicator present at all. Here we simply do the same by using an infinitesimally small amount of dye in the simulation. With a known Δ[Ca^{2+}]$_{total}$ of 50 μM this means that fast buffer capacity (κ) of the whole system (including fast buffering by CB and the C-terminus) is 19, which is comparable to values found for fast buffering in spines of CA1 pyramidal cells [5,25].

Supplementary data 6. Fast Ca^{2+} buffering by ATP

It has been suggested that ATP can contribute significantly to the fast buffering capacity of a cell[28]. To investigate this possibility, we repeated the 50 μM Ca^{2+} influx in the model (with CaM and CB) with ATP added to the system. For the properties of ATP we used $K_{dCa(^{2+})}$=200 μM, $K_{dMg(^{2+})}$=100 μM and $k_{onCa(^{2+})}$=2×10^8 $M^{-1}s^{-1}$ [28]. The binding and unbinding rates of Mg^{2+} to ATP were considered too slow to play a significant role in the studied timespan[28]. With 4 mM MgATP [4,28], and 100 nM free Ca^{2+}, 580 μM ATP will be free and available to buffer a rise in Ca^{2+}. Under these conditions, the Ca^{2+} signal observed with OGB-1 is only slightly smaller compared to the situation without ATP (Supplementary Fig. 7a, solid blue vs. red line). The κ determined from the system with 580 μM free ATP only increases from 19 to 22 (Supplementary Fig. 7b). In comparison, when the simulation was repeated with no CaM and only ATP as a fast buffer, the observed $[Ca^{2+}]$peak was >8 μM (Supplementary Fig. 7a solid green line) indicating this system had a buffering capacity of κ=4 (Supplementary Fig. 7b), which is substantially smaller compared to values found for fast buffering in spines of CA1 pyramidal cells measured with OGB-1 (κ=~20) [5,25]. Clearly ATP under these conditions (4 mM $[MgATP]_{total}$) will only minimally contribute to the buffering capacity. We attempted to actually measure the kinetic properties of Ca^{2+} binding to ATP and found it to be technically extremely difficult because CaATP and MgATP can form complexes with zwitterions such as pH buffers like HEPES[29] that are generally used in biological research:

$$\left[Ca^{2+}\right]+\left[ATP\right]\underset{K_d=200\,\mu M}{\rightleftharpoons}\left[CaATP\right]+\left[HEPES\right]\underset{K_d=1mM}{\rightleftharpoons}\left[CaATPHEPES\right] \quad \text{(eq. S8)}$$

$$\left[Mg^{2+}\right]+\left[ATP\right]\underset{K_d=100\,\mu M}{\rightleftharpoons}\left[MgATP\right]+\left[HEPES\right]\underset{K_d=1mM}{\rightleftharpoons}\left[MgATPHEPES\right] \quad \text{(eq. S9)}$$

It is important for our measurements that the pH is strongly buffered since the kinetic properties on CBPs strongly depend on pH, and pH changes upon uncaging of DMn. Normally, we use a high concentration of HEPES which would further complicate dynamic measurements of Ca^{2+} binding to ATP making it impossible to measure it in this way. To ensure a stable acidity, HEPES is very often used in experiments as a pH buffer [4,5,30]. , In the experiments[30] from which it was suggested that ATP can significantly contribute to the fast Ca^{2+} buffering capacity of a cell 10 mM HEPES was used. Unfortunately, this amount of HEPES was not accounted for when estimating the free [ATP][28]. Using an estimated a K_d of 1 mM for HEPES to either CaATP and MgATP[29], we calculated that 220 μM ATP is free to buffer the Ca^{2+} rise in the presence of 10 mM HEPES total, 4 mM MgATP total and 100 nM free Ca^{2+}. This means that with 4 mM MgATP and 10 mM HEPES added[4,5,30] for the system modeled here (with 100 μM CaM and 30 μM CB) the Ca^{2+} signal measured with OGB-1 to a $\Delta[Ca^{2+}]_{total}$ of 50 μM would be almost identical to a system without the ATP (Supplementary Fig. 7a, long dash blue). The κ only increases from 19 to 20 in the system without ATP (Supplementary Fig. 7b, large dot blue). Moreover, in unperturbed cells the $[ATP]_{total}$ is around 0.9 mM [31] and the $[Mg^{2+}]_{free}$ around 1 mM [32,33] which would leave only 58 μM ATP to buffer incoming Ca^{2+}, leading to a negligible increase in buffering capacity (Supplementary Fig. 7a and b, short dash/small dot blue). By itself ATP has some buffering capacity (Supplementary Fig. 7b, green).

Therefore, it will account for some of the fast buffering of CaM (Supplementary Fig. 7c) and will slightly increase the capacity of a whole system with CaM and CB present. However, the contribution is minimal under most experimental conditions (with HEPES) and negligible in unperturbed cells.

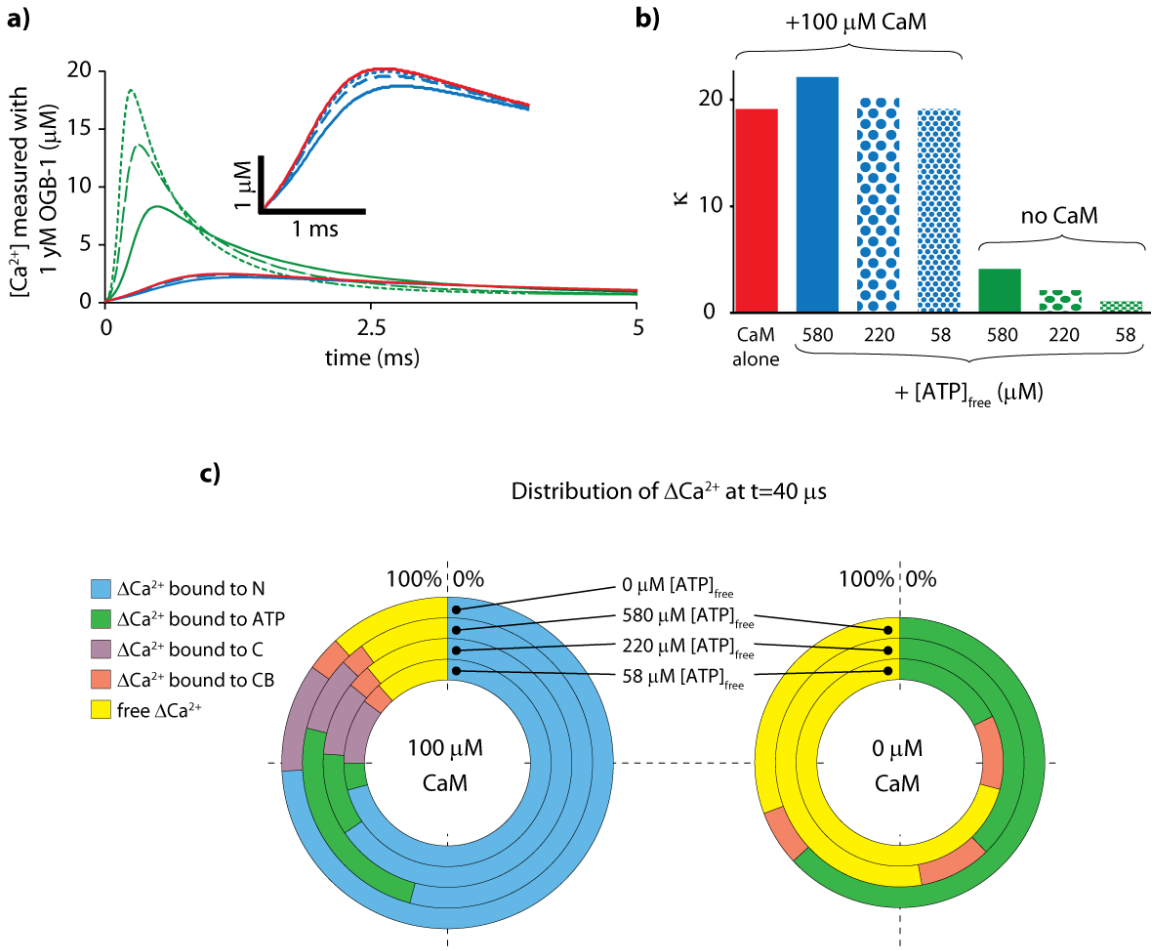

Supplementary Figure 7. ATP as a fast Ca^{2+} buffer. Single-compartment simulations of Ca^{2+} dynamics in a dendritic spine of a hippocampal CA1 pyramidal cell containing 100 μM CaM, 30 μM CB and varying amounts of free ATP. At t=0, $[Ca^{2+}]_{total}$ was rapidly (τ=10 μs) increased by 50 μM. a) $[Ca^{2+}]_{free}$ as it would be measured with 1 yM OGB-1 ($[Ca^{2+}]_{OGB-1}$ with no ATP (red), 580 μM (solid blue), 220 μM (long dash blue) and 58 μM (short dash blue) free ATP present. These are the expected values of free ATP under the recording conditions of 4 mM $[MgATP]_{total}$ and 4 mM $[MgATP]_{total}$ with 10 mM $[HEPES]_{total}$ and the physiological condition of 0.9 mM $[ATP]_{total}$ with 1 mM $[Mg^{2+}]_{free}$ (respectively). For comparison, simulations are also shown of the $[Ca^{2+}]_{OGB-1}$ when no CaM is present (green lines). b) From the $[Ca^{2+}]_{OGB-1}$ curves the buffer capacity (κ) only slightly increases due to the addition of ATP to the system (compare red to blue bars) as the buffering capacity of the ATP by itself is minimal (green bars). ATP does take over some of the fast buffering by CaM as shown in the distribution of the added Ca^{2+} after 40 μs (c left figure). However, when CaM was taken out of the system there is a substantial increase in unbuffered Ca^{2+} at t=40 μs (c right figure).

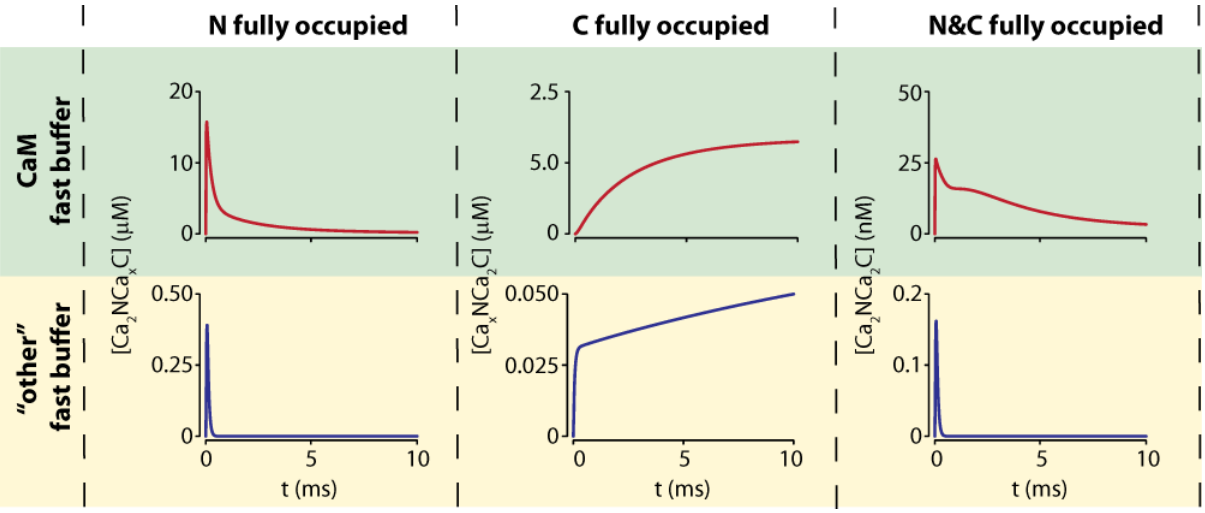

Supplementary Figure 8. **Comparing new CaM kinetics with those used in previous studies.** With the N-lobe having such a high speed of binding and Ca^{2+} 'flowing' from N-lobe to C-lobe to a high affinity CBP (see Fig 2b in main text) much more Ca^{2+} will be bound to CaM then expected with the previously assumed properties of CaM. We simulated a 50 μM increase in total [Ca^{2+}] from an initial condition of 100 nM free [Ca^{2+}]. To compare how CaM is activated having the newly determined properties to its properties described earlier, we simulated the CaM in two ways. We simulated CaM as determined in the present study (top row, CaM fast buffer) to contrast it to CaM with properties used in earlier simulations[34] (bottom row, "other" fast buffer). In earlier simulations 260 μM CaM and 45 μM CB together with 5 μM 'fast buffer' was assumed[34]. To make a fair comparison, we simulated the newly determined CaM properties also at 260 μM CaM and 45 μM CB (but added no 'fast buffer'). It is difficult to define exactly when CaM is "activated" since some processes only need Ca^{2+} binding to the N-lobe or C-lobe whereas other CaM targets need fully occupied CaM (both lobes) to be activated. Therefore, we simulated here the concentrations of fully occupied N-lobes, C-lobes and whole CaM (both lobes) that occur in the first 10 ms after the influx of Ca^{2+}. Please note that the y-axis scales between the old CaM properties (bottom row) and new CaM properties (top row) are one to two orders of magnitude different.

Supplementary figure legend. A more detailed description of figure 2 in the main text

In figure 2 a single neuronal compartment was simulated with a buffer composition as expected in CA1 pyramidal cells. In this compartment with 100 μM CaM and 30 μM CB the $[Ca^{2+}]$ was very rapidly (τ=10 μs) increased by 50 μM ($\Delta[Ca^{2+}]_{total}$). At 20 μs (the maximum time resolution in the figure is 20 μs) $\Delta[Ca^{2+}]_{free}$ peaks at 8.8 μM. As the total $[Ca^{2+}]$ increases, the bulk of the $\Delta[Ca^{2+}]_{total}$ is rapidly bound to the N-terminus of CaM. At ~40 μs, 36.4 μM Ca^{2+} (73% of $\Delta[Ca^{2+}]_{total}$) is bound to the N-terminus ($\Delta[Ca^{2+}]_N$), while at that moment 5.2 μM (10% of $\Delta[Ca^{2+}]_{total}$) and 1.7 μM (3.3% of $\Delta[Ca^{2+}]_{total}$) are bound to the C-terminus ($\Delta[Ca^{2+}]_C$) and CB ($\Delta[Ca^{2+}]_{CB}$) respectively. After this, the $\Delta[Ca^{2+}]_N$ drops with two τ's of 0.38 ms (64%) and 2.1 ms (36%) to 0.54 μM (1.1% of $\Delta[Ca^{2+}]_{total}$) at 30 ms. Around 0.9 ms the $\Delta[Ca^{2+}]_C$ reaches its maximum of 21.4 μM (43% of $\Delta[Ca^{2+}]_{total}$) while at that moment there is 11.0 μM $\Delta[Ca^{2+}]_N$ (22% C and 14.9 μM $\Delta[Ca^{2+}]_{CB}$ (30% of ($\Delta[Ca^{2+}]_{total}$). After this peak the $\Delta[Ca^{2+}]_C$ drops with a τ of 3.7 ms to 9.8 μM (19.7% of $\Delta[Ca^{2+}]_{total}$) at 30 ms. Over the whole experimental period, the $[Ca^{2+}]_{CB}$ steadily increases with τ's of 0.63 ms (27%) and 3.1 ms (73%) to 39.3 μM (78.6% of $\Delta[Ca^{2+}]_{total}$) at 30 ms. With 99.3% $\Delta[Ca^{2+}]_{total}$ bound to either the N-terminus, C-terminus or CB 0.35 μM of $\Delta[Ca^{2+}]_{total}$ (i.e., 0.7%) remains unbound after 30 ms.

b) To better understand how Ca^{2+} moves through the system composed of 3 buffers, the amount of Ca^{2+} flowing between the four states, free ($\Delta[Ca^{2+}]_{free}$), bound to the N-terminus ($\Delta[Ca^{2+}]_N$), bound to the C-terminus ($\Delta[Ca^{2+}]_C$) and bound to CB ($\Delta[Ca^{2+}]_{CB}$) were calculated for 3 epochs. The concentrations of Ca^{2+} in the different states is represented by the area covered by the different circles where the grey area represents the concentration at the beginning of the epoch, while the colored circles represent the concentration at the end of the epoch. The numbers in the figure indicate percent of $\Delta[Ca^{2+}]_{total}$. During the first epoch (red), which runs from the start of the simulation (t=0 s) to when $[Ca^{2+}]_N$ peaks (t=40 μs) 86.6% of the 50 μM $\Delta[Ca^{2+}]_{total}$ (top grey circle) is directly bound by the 3 buffers (78.7% $[Ca^{2+}]_N$, 6.0% $[Ca^{2+}]_C$ and 1.9% $[Ca^{2+}]_{CB}$). Small amounts of buffered Ca^{2+} are already redistributed from $[Ca^{2+}]_N$ to $[Ca^{2+}]_N$ (4.4%) and $[Ca^{2+}]_{CB}$ (1.5%). During the second epoch (green), which runs from 40 μs to when $[Ca^{2+}]_C$ peaks (t=900 μs), and the last epoch (green, 0.9–30 ms) a further total of 11.7% of free Ca^{2+} is directly bound by the N-terminus whereas the amounts of free Ca^{2+} directly binding to either C-terminus (0.8%) or CB (0.2%) are less than 1% and for clarity are not shown. After the first 40 μs the main 'flow' of Ca^{2+} is the redistribution between the 3 buffering components. During the second epoch 33.0% moves from $[Ca^{2+}]_N$ to $[Ca^{2+}]_C$, 25.3% from $[Ca^{2+}]_N$ to $[Ca^{2+}]_{CB}$ and 1.0% from $[Ca^{2+}]_C$ to $[Ca^{2+}]_{CB}$. Remarkably, during the third epoch 19.3% moves back from $[Ca^{2+}]_C$ to $[Ca^{2+}]_N$ which is then directly redistributed to the C-terminus as part of the 44.4% that moves from $[Ca^{2+}]_N$ to $[Ca^{2+}]_{CB}$. Also a further 4.2% moves from $[Ca^{2+}]_C$ to $[Ca^{2+}]_{CB}$. All the net redistributions that take place during the 30 ms of the simulation are shown in the diagram with the black arrows where the black circles correlate with the end concentration and the white circles indicate the maxima reached during the experiment. Over the whole period more than 89% of the $\Delta[Ca^{2+}]_{total}$ is first bound by the fast

N-terminus which is later bound to the slower C-terminus and CB which eventually outcompete the N-terminus based on their higher affinity for Ca^{2+}.

References to Supplementary Information

1 Berggard, T. *et al.* Calbindin D28k exhibits properties characteristic of a Ca^{2+} sensor. *J.Biol.Chem.* **277**, 16662–16672 (2002).

2 Nagerl, U. V., Novo, D., Mody, I. & Vergara, J. L. Binding kinetics of calbindin-D(28k) determined by flash photolysis of caged Ca($^{2+}$). *Biophys J* **79**, 3009–3018, doi:S0006-3495(00)76537–4 [pii] 10.1016/S0006-3495(00)76537–4 (2000).

3 Faas, G. C., Karacs, K., Vergara, J. L. & Mody, I. Kinetic properties of DM-nitrophen binding to calcium and magnesium. *Biophys J* **88**, 4421–4433, doi:S0006-3495(05)73489–5 [pii] 10.1529/biophysj.104.057745 (2005).

4 Sabatini, B. L., Oertner, T. G. & Svoboda, K. The life cycle of Ca($^{2+}$) ions in dendritic spines. *Neuron* **33**, 439–452, doi:S0896627302005731 [pii] (2002).

5 Cornelisse, L. N., van Elburg, R. A., Meredith, R. M., Yuste, R. & Mansvelder, H. D. High speed two-photon imaging of calcium dynamics in dendritic spines: consequences for spine calcium kinetics and buffer capacity. *PLoS ONE* **2**, e1073, doi:10.1371/journal.pone.0001073 (2007).

6 McIlwain, H. & Bachelard, H. S. *Biochemistry and the central nervous system*. 5th edn, (Churchill Livingstone, 1985).

7 Banay-Schwartz, M., Kenessey, A., DeGuzman, T., Lajtha, A. & Palkovits, M. Protein content of various regions of rat brain and adult aging human brain. *Age* **15**, 51–54 (1992).

8 Pond, W. G. *et al.* Severe protein deficiency and repletion alter body and brain composition and organ weights in infant pigs. *J Nutr* **126**, 290–302 (1996).

9 Mori, M. X., Erickson, M. G. & Yue, D. T. Functional stoichiometry and local enrichment of calmodulin interacting with Ca^{2+} channels. *Science* **304**, 432–435 (2004).

10 Kubota, Y., Putkey, J. A. & Waxham, M. N. Neurogranin controls the spatiotemporal pattern of postsynaptic Ca^{2+}/CaM signaling. *Biophys J* **93**, 3848–3859, doi:S0006-3495(07)71639–9 [pii] 10.1529/biophysj.107.106849 (2007).

11 Nicholson, C. & Sykova, E. Extracellular space structure revealed by diffusion analysis. *Trends Neurosci* **21**, 207–215, doi:S0166-2236(98)01261–2 [pii] (1998).

12 Reinoso, R. F., Telfer, B. A. & Rowland, M. Tissue water content in rats measured by desiccation. *J Pharmacol Toxicol Methods* **38**, 87–92, doi:S1056-8719(97)00053–1 [pii] (1997).

13 Altman, P. L. & Katz, D. D. *Biology data book*. 2d edn, (Federation of American Societies for Experimental Biology, 1972).

14 Klee, C. B. & Vanaman, T. C. Calmodulin. *Adv Protein Chem* **35**, 213–321 (1982).

15 Kakiuchi, S. *et al.* Quantitative determinations of calmodulin in the supernatant and particulate fractions of mammalian tissues. *J Biochem* **92**, 1041–1048 (1982).

16 Biber, A., Schmid, G. & Hempel, K. Calmodulin content in specific brain areas. *Exp Brain Res* **56**, 323–326 (1984).

17 Vargas, F. & Guidotti, A. Calmodulin in brain of schizophrenics. *Neurochem Res* **5**, 673–681 (1980).

18 Sano, M. & Kitajima, S. Ontogeny of calmodulin and calmodulin-dependent adenylate cyclase in rat brain. *Brain Res* **283**, 215–220 (1983).

19 Kitajima, S., Seto-Ohshima, A., Sano, M. & Kato, K. Production of antibodies to calmodulin in rabbits and enzyme immunoassays for calmodulin and anti-calmodulin. *J Biochem* **94**, 559–564 (1983).

20 Teolato, S., Calderini, G., Bonetti, A. C. & Toffano, G. Calmodulin content in different brain areas of aging rats. *Neurosci Lett* **38**, 57–60, doi:0304-3940(83)90110–6 [pii] (1983).

21 Lin, C. T., Dedman, J. R., Brinkley, B. R. & Means, A. R. Localization of calmodulin in rat cerebellum by immunoelectron microscopy. *J Cell Biol* **85**, 473–480 (1980).

22 Neher, E. & Augustine, G. J. Calcium gradients and buffers in bovine chromaffin cells. *J.Physiol* **450**, 273–301 (1992).

23 Helmchen, F., Imoto, K. & Sakmann, B. Ca^{2+} buffering and action potential-evoked Ca^{2+} signaling in dendrites of pyramidal neurons. *Biophys J* **70**, 1069–1081, doi:S0006-3495(96)79653–4 [pii] 10.1016/S0006-3495(96)79653–4 (1996).

24 Lee, S. H., Rosenmund, C., Schwaller, B. & Neher, E. Differences in Ca^{2+} buffering properties between excitatory and inhibitory hippocampal neurons from the rat. *J Physiol* **525 Pt 2**, 405–418, doi:PHY_9975 [pii] (2000).

25 Sabatini, B. L., Oertner, T. G. & Svoboda, K. The life cycle of Ca^{2+} ions in dendritic spines. *Neuron* **33**, 439–452 (2002).

26 Einstein, A. The motion of elements suspended in static liquids as claimed in the molecular kinetic theory of heat. *Ann. Phys.-Berlin* **17**, 549–560 (1905).

27 Smoluchowski, M. Theory of the Brownian movements. *Bulletin de l'Academie des Sciences de Cracovie|Bulletin de l'Academie des Sciences de Cracovie|Annalen der Physik*, 577–602|756–780 (1906).

28 Meinrenken, C. J., Borst, J. G. & Sakmann, B. Calcium secretion coupling at calyx of held governed by nonuniform channel-vesicle topography. *J Neurosci* **22**, 1648–1667, doi:22/5/1648 [pii] (2002).

29 Azab, H. A., Orabi, A. S. & El-Salam, E. T. A. Role of biologically important zwitterionic buffer secondary ligands on the stability of the mixed-ligand complexes of divalent metal ions and adenosine 5 '-mono-, 5 '-di-, and 5 '-triphosphate. *Journal of Chemical and Engineering Data* **46**, 346–354, doi:Doi 10.1021/Je0001779 (2001).

[30] Borst, J. G., Helmchen, F. & Sakmann, B. Pre- and postsynaptic whole-cell recordings in the medial nucleus of the trapezoid body of the rat. *J Physiol* **489 (Pt 3)**, 825–840 (1995).

[31] Ainscow, E. K., Mirshamsi, S., Tang, T., Ashford, M. L. & Rutter, G. A. Dynamic imaging of free cytosolic ATP concentration during fuel sensing by rat hypothalamic neurones: evidence for ATP-independent control of ATP-sensitive K(+) channels. *J Physiol* **544**, 429–445, doi:PHY_022434 [pii] (2002).

[32] Brocard, J. B., Rajdev, S. & Reynolds, I. J. Glutamate-induced increases in intracellular free Mg^{2+} in cultured cortical neurons. *Neuron* **11**, 751–757, doi:0896-6273(93)90084–5 [pii] (1993).

[33] Grubbs, R. D. Intracellular magnesium and magnesium buffering. *Biometals* **15**, 251–259 (2002).

[34] Keller, D. X., Franks, K. M., Bartol, T. M., Jr. & Sejnowski, T. J. Calmodulin activation by calcium transients in the postsynaptic density of dendritic spines. *PLoS ONE* **3**, e2045, doi:10.1371/journal.pone.0002045 (2008).

[35] Faas, G. C., Schwaller, B., Vergara, J. L. & Mody, I. Resolving the fast kinetics of cooperative binding: Ca^{2+} buffering by calretinin. *PLoS Biol* **5**, e311, doi:07-PLBI-RA-1024 [pii] 10.1371/journal.pbio.0050311 (2007).